

Article

# Fabrication of C/Co-FeS<sub>2</sub>/CoS<sub>2</sub> with Highly Efficient Hydrogen Evolution Reaction

Yuan Gao <sup>1,†</sup>, Ka Wang <sup>1,†</sup>, Haizeng Song <sup>2</sup>, Han Wu <sup>2</sup>, Shancheng Yan <sup>1,\*</sup> , Xin Xu <sup>1</sup> and Yi Shi <sup>2,\*</sup>

<sup>1</sup> School of Geography and Biological Information, Nanjing University of Posts and Telecommunications, Nanjing 210023, China; gaoynjupt@163.com (Y.G.); wknjupt121706@163.com (K.W.); xuxin@njupt.edu.cn (X.X.)

<sup>2</sup> School of Electronic Science and Engineering, Nanjing University, Nanjing 210093, China; njushz@163.com (H.S.); hanshanchier@berkeley.edu (H.W.)

\* Correspondence: yansc@njupt.edu.cn (S.Y.); yshi@nju.edu.cn (Y.S.)

† Yuan Gao and Ka Wang contribute equally to this work.

Received: 24 May 2019; Accepted: 19 June 2019; Published: 21 June 2019



**Abstract:** The mainstream strategy for designing hydrogen electrocatalysts is to adjust their surface electronic structure; however, the conductivity of the electrocatalyst and the synergy with its substrate are still challenges to overcome. In this work, we report a carbon-doped Co-FeS<sub>2</sub>/CoS<sub>2</sub> (C/Co-FeS<sub>2</sub>/CoS<sub>2</sub>) electrode, prepared via a hydrothermal process with carbon cloth (CC) as the substrate and carbon doping. The C/Co-FeS<sub>2</sub>/CoS<sub>2</sub> electrode shows excellent catalytic activity in the hydrogen evolution reaction (HER) with an overpotential of 88 mV at a current density of  $-10 \text{ mA}\cdot\text{cm}^{-2}$  in 0.5 M H<sub>2</sub>SO<sub>4</sub> solution. The Tafel slope is  $66 \text{ mV}\cdot\text{dec}^{-1}$ . Such superior performance is attributed to the high electrical conductivity of the electrocatalyst and its synergy with the substrate. Our study provides an efficient alternative in the field of electrocatalysis.

**Keywords:** carbon-doped; electrocatalyst; C/Co-FeS<sub>2</sub>/CoS<sub>2</sub>; HER

## 1. Introduction

Sustainable energy played a crucial role in the past few decades. In contrast with the traditional energy industry, clean energy attracts attention for its environmentally friendly nature, abundance, and renewability [1–9]. Water splitting is the most promising method for sustainable hydrogen preparation [4,10–12]. The current status of platinum-based and palladium-based electrocatalysis for water splitting exhibits good hydrogen evolution performance; however, the high cost and low earth abundance seriously hinder the large-scale application of precious metal electrocatalysts [1,12–17]. Non-precious metal electrocatalysts received great attention, but the catalytic performance of non-precious metal electrocatalysts is still far from that of noble metal catalysts [18–23].

Non-precious metal chalcogenides are considered a class of very promising candidates for the hydrogen evolution reaction (HER) due to their high abundance, low cost, and thermal and mechanical stability [13–16]. However, practical applications of non-precious metal chalcogenides as HER cathode materials are limited by their low electrical conductivity and lack of active sites. In our previous research, we demonstrated good electrocatalytic properties of Co-doped FeS<sub>2</sub>, and CoS<sub>2</sub> formed heterostructures on Co-FeS<sub>2</sub> petals that can be attributed to the unique three-dimensional hierarchy. For example, the use of carbon materials solely as conductive substrates does not significantly improve the performance of the electrocatalysts [11,24]. If the carbon-doped non-precious metal catalyst is grown on the conductive substrate, its catalytic performance will be greatly improved due to the improvement of the conductivity of Co-FeS<sub>2</sub>/CoS<sub>2</sub> and its interaction with the substrate [25–27].

In this study, we used glucose as a carbon source to synthesize carbon doped Co-FeS<sub>2</sub>/CoS<sub>2</sub> (C/Co-FeS<sub>2</sub>/CoS<sub>2</sub>) on carbon cloth via a one-step hydrothermal method. The resulting electrode shows excellent HER catalytic activity with an overpotential of 88 mV at a current density  $-10 \text{ mA}\cdot\text{cm}^{-2}$  in 0.5 M H<sub>2</sub>SO<sub>4</sub> solution; this is 15 mV lower than the overpotential of our previous research [19]. Because of the incorporation of carbon that results in synergistic catalysis between carbon and Co-aFeS<sub>2</sub>/CoS<sub>2</sub>, the performance of the catalyst is significantly improved due to the improvement in conductivity of C/Co-FeS<sub>2</sub>/CoS<sub>2</sub> and the reduction of resistance between C/Co-FeS<sub>2</sub>/CoS<sub>2</sub> and the substrate [27–32]. This study of doping non-metallic elements into non-precious catalysts provides a simple and efficient way to improve performance in the field of electrocatalysis.

## 2. Result and Discussion

In this work, we obtained C/Co-FeS<sub>2</sub>/CoS<sub>2</sub> with better performance by incorporating carbon on the basis of our previous research. The typical morphology of C/Co-FeS<sub>2</sub>/CoS<sub>2</sub> was revealed by scanning electron microscopy images, as presented in Figure 1. The micro-spherical structure of C/Co-FeS<sub>2</sub>/CoS<sub>2</sub> shown in Figure 1a,b typically ranged from 500 nm to 1  $\mu\text{m}$  in diameter. Figure 1c,d show the SEM images and energy-dispersive spectrometry (EDS) elemental mapping of C, Fe, Co, and S for C/Co-FeS<sub>2</sub>/CoS<sub>2</sub>, which confirmed the existence of these elements and also suggested that carbon existed in the C/Co-FeS<sub>2</sub>/CoS<sub>2</sub> [11]. Figure S1 (Supplementary Materials) shows a larger-scale element distribution, which further demonstrates the uniformity of the electrocatalyst on the whole carbon fiber. Figure S2 (Supplementary Materials) shows the SEM images of C/CoS<sub>2</sub>, C/FeS<sub>2</sub>, and carbon (C) with particle sizes of 10 to 13  $\mu\text{m}$ , 300 to 400 nm, and 150 to 250 nm, respectively. The addition of carbon led to the micro-spherical morphology of C/FeS<sub>2</sub> and C/CoS<sub>2</sub>.

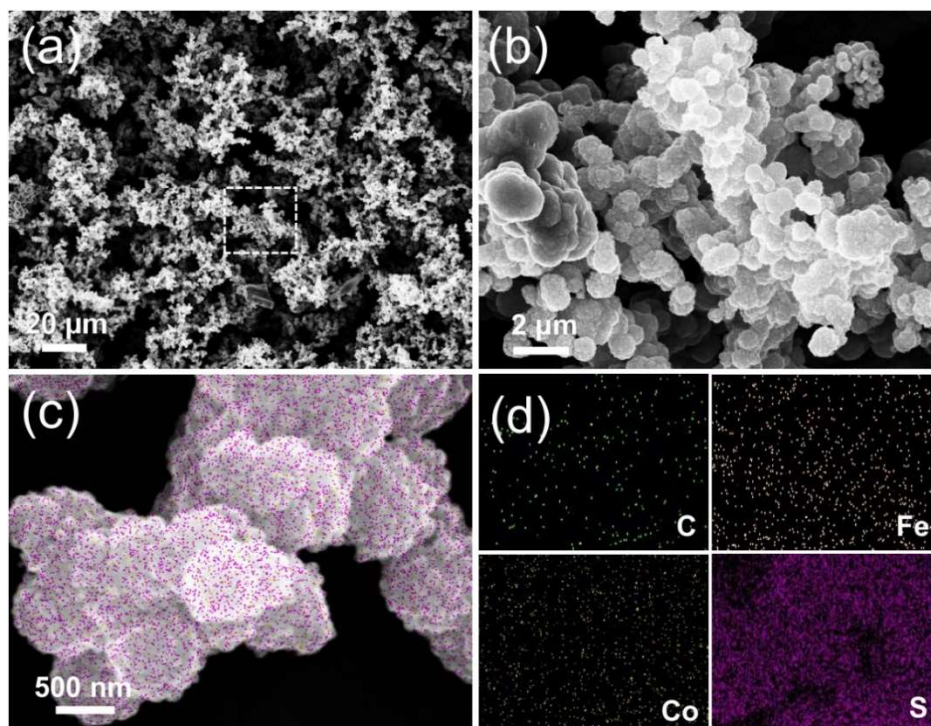


**Figure 1.** (a–c) Scanning electron microscopy images of C/Co-FeS<sub>2</sub>/CoS<sub>2</sub>; (d) corresponding energy-dispersive spectroscopy (EDS) elemental mapping images of C, Fe, Co, and S for C/Co-FeS<sub>2</sub>/CoS<sub>2</sub>.

In addition, we further examined the crystal structure of the sample by X-ray diffraction (XRD) and Raman spectroscopy. Figure 2a is the XRD pattern for C/Co-FeS<sub>2</sub>/CoS<sub>2</sub>, where the diffraction peaks at 28.4°, 32.9°, 37°, 40.7°, 47.3°, and 56.1° can be precisely indexed to planes of FeS<sub>2</sub> (JCPDS#42-1340) at (111), (200), (210), (211), (220), and (311). Only some weaker peaks belong to CoS<sub>2</sub>

(JCPDS#41-1471) [13,22,23]. The peak at  $26.5^\circ$  corresponds to the bare carbon fiber, which is supplied in the XRD text. The XRD results clearly reveal that C/Co-FeS<sub>2</sub>/CoS<sub>2</sub> has a complete nanocrystalline phase. Figure 2b is the Raman spectrum of the C/Co-FeS<sub>2</sub>/CoS<sub>2</sub>. The two peaks at  $335\text{ cm}^{-1}$  and  $371\text{ cm}^{-1}$  exhibited by C/Co-FeS<sub>2</sub>/CoS<sub>2</sub> are due to the incorporation of carbon into Co-FeS<sub>2</sub>/CoS<sub>2</sub>. Two carbon peaks were also observed at the D peak ( $1351\text{ cm}^{-1}$ ) and G peak ( $1490\text{ cm}^{-1}$ ), where the position of the G peak is determined by the amount of hydrogen from the carbon–hydrogen bond [33]. To further demonstrate the structure of C/Co-FeS<sub>2</sub>/CoS<sub>2</sub>, transmission electron microscopy (TEM) was employed, as shown in Figure 2c,d and Figure S3 (Supplementary Materials) are high-resolution TEM (HRTEM) images, indicating that the carbon element was mainly located at the outer edge of the C/Co-FeS<sub>2</sub>/CoS<sub>2</sub> nanostructure, while the inset shows the selected area electron diffraction (SAED) patterns of C/Co-FeS<sub>2</sub>/CoS<sub>2</sub>, indicating the formation of a good crystal structure. The inter-planar spacing (210) of FeS<sub>2</sub> was 0.24 nm and the spacing (210) of CoS<sub>2</sub> was 0.25 nm. The existence of carbon can be proven from this pattern that had inter-planar spacing of about 0.34 nm.

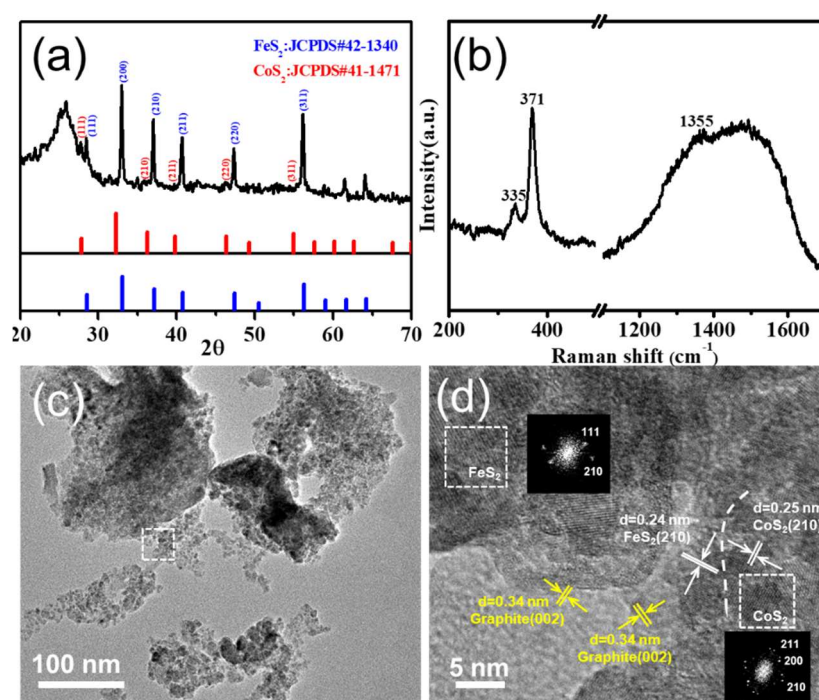


**Figure 2.** (a) X-ray diffraction (XRD) pattern of C/Co-FeS<sub>2</sub>/CoS<sub>2</sub>; (b) Raman spectroscopy pattern of C/Co-FeS<sub>2</sub>/CoS<sub>2</sub>; (c) transmission electron microscopy (TEM) image of C/Co-FeS<sub>2</sub>/CoS<sub>2</sub>; (d) high-resolution TEM (HRTEM) image of C/Co-FeS<sub>2</sub>/CoS<sub>2</sub> (the insets show the SAED patterns).

To understand the elemental valence and chemical composition of C/Co-FeS<sub>2</sub>/CoS<sub>2</sub>, we conducted X-ray photoelectron spectroscopy (XPS) measurements. Figure 3a shows the full XPS survey spectra of C/Co-FeS<sub>2</sub>/CoS<sub>2</sub>. Figure 3b is the XPS spectrum of the C element. In Figure 3c, the two peaks at 708 eV and 720 eV correspond to Fe 2p<sub>3/2</sub> and Fe 2p<sub>1/2</sub>. The other peaks at 712 and 726.6 eV correspond to Fe 2p<sub>3/2</sub> and Fe 2p<sub>1/2</sub> of C/Co-FeS<sub>2</sub>/CoS<sub>2</sub>, which had a positive shift as compared with FeS<sub>2</sub>, due to the formation of an interface between FeS<sub>2</sub> and CoS<sub>2</sub> [15]. The XPS spectrum of Co shown in Figure 3d consists of two peaks at 778.8 eV for Co 2p<sub>3/2</sub> and 793.5 eV for Co 2p<sub>1/2</sub>, with two shake-up satellites [16]. The binding energies of S 2p<sub>3/2</sub> at 162.6 eV belong to S<sub>2</sub><sup>2-</sup> of CoS<sub>2</sub>, whereas the binding energies of S 2p<sub>1/2</sub> at around 163.8 eV correspond to S<sub>2</sub><sup>2-</sup> of Co-FeS<sub>2</sub>, and the peak at around 168.3 eV is attributed to oxidized S species [16,18,19].

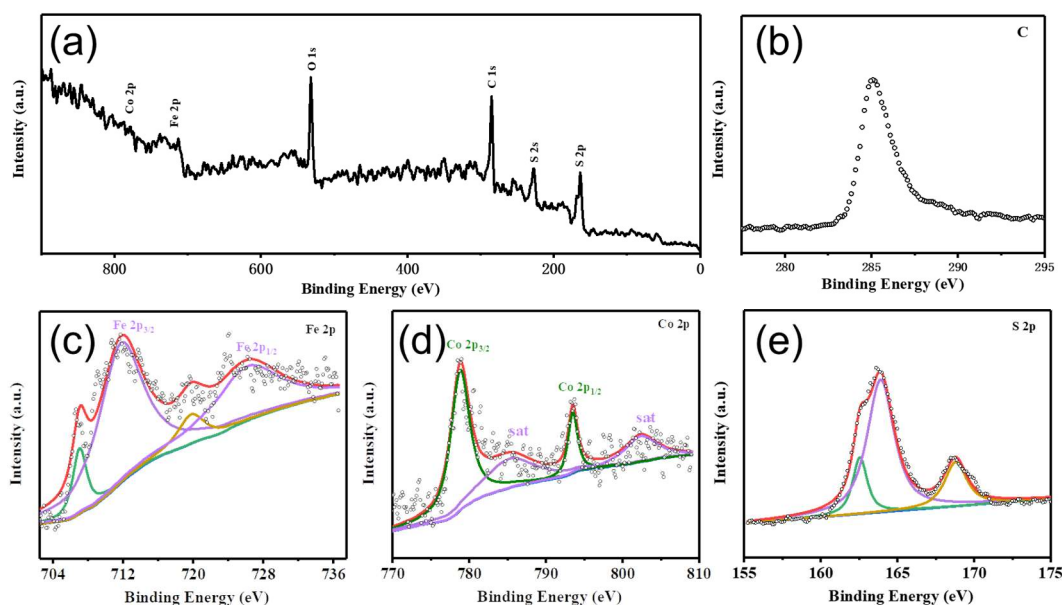


**Figure 3.** (a) X-ray photoelectron spectroscopy (XPS) survey spectrum for C/Co-FeS<sub>2</sub>/CoS<sub>2</sub>; XPS spectra of C/Co-FeS<sub>2</sub>/CoS<sub>2</sub> from (b) C, (c) Fe 2p, (d) Co 2p, and (e) S 2p.

HER activity was analyzed by measuring the linear sweep voltammetry (LSV) curve of C/Co-FeS<sub>2</sub>/CoS<sub>2</sub> in a 0.5 M H<sub>2</sub>SO<sub>4</sub> solution. The performances of C/CoS<sub>2</sub>, C/FeS<sub>2</sub>, C, and bare CC were also analyzed under the same conditions as shown in Figure 4a. The bare CC showed almost no catalytic activity. However, C/Co-FeS<sub>2</sub>/CoS<sub>2</sub> grown on CC substrates showed excellent HER activity, and had a lower overpotential ( $\eta = 88$  mV) at a current density of  $-10$  mA·cm<sup>-2</sup>, much smaller than C/CoS<sub>2</sub> (113 mV) and C/FeS<sub>2</sub> (177 mV), as shown in Figure 4a. We summarized the opening voltage of the hydrogen evolution reaction of similar catalysts that were published so far, and found that C/Co-FeS<sub>2</sub>/CoS<sub>2</sub> had the best performance, as shown in Figure S4 (Supplementary Materials) [18,19,22,34,35]. The Tafel slope of C/Co-FeS<sub>2</sub>/CoS<sub>2</sub> ( $66$  mV·dec<sup>-1</sup>) was smaller than that of C/CoS<sub>2</sub> ( $77$  mV·dec<sup>-1</sup>) and C/FeS<sub>2</sub> ( $119$  mV·dec<sup>-1</sup>), as shown in Figure 4b. It is worth noting that the electrocatalyst formed on the carbon cloth after the simple glucose reaction showed significant catalytic activity compared with the blank carbon cloth. The [R(C(RW))] circuit can be obtained by simulating the electrochemical impedance spectroscopy (EIS) data in Figure S6 (Supplementary Materials). As shown in the circuit diagram of Figure S6b (Supplementary Materials),  $R_s$ ,  $R_{ct}$ ,  $C$ , and  $W$  represent bulk solution resistance, charge-transfer resistance, capacitance, and Warburg resistance, respectively. By comparing the simulated data, it can be found that C/Co-FeS<sub>2</sub>/CoS<sub>2</sub> ( $0.14$   $\Omega$ ) showed a much smaller resistance in the Nyquist diagram than C/CoS<sub>2</sub> ( $0.19$   $\Omega$ ) and C/FeS<sub>2</sub> ( $0.54$   $\Omega$ ). Figure 4c indicates the stability of C/Co-FeS<sub>2</sub>/CoS<sub>2</sub>; 8 mV of the overpotential was lost after 500 cycles. In addition, as shown in Figure S7 (Supplementary Materials), C/Co-FeS<sub>2</sub>/CoS<sub>2</sub> hardly changed its microscopic morphology after 500 cycles of cyclic voltammetry (CV). It can be seen from the comparison that there was no significant change in the overall surface of the C/Co-FeS<sub>2</sub>/CoS<sub>2</sub> nanosphere after a 500-cycle durability test in an acidic solution, with only slight corrosion marks. To analyze the activity of C/Co-FeS<sub>2</sub>/CoS<sub>2</sub>, we calculated non-faradaic double-layer capacitance ( $C_{dl}$ ) by cyclic voltammetry measurements at different scan rates (5, 10, 20, 30, 40, 50, 60, 70, 80, 90, and 100 mV·s<sup>-1</sup>) to obtain the electrochemical surface area (ECA). The catalytic performances of the working electrode were normalized to 1 cm<sup>2</sup>. Data of the cyclic voltammetry measurements at different scan rates are shown in Figure S5 (Supplementary Materials). It was calculated that the  $C_{dl}$  of C/Co-FeS<sub>2</sub>/CoS<sub>2</sub> was 129 mF·cm<sup>-2</sup>, which is much larger than the 43 mF·cm<sup>-2</sup> of C/FeS<sub>2</sub> and 23 mF·cm<sup>-2</sup> of C/CoS<sub>2</sub>. Although the  $C_{dl}$  of C was only 1.2 mF·cm<sup>-2</sup>, it can be said that the carbon obtained after the glucose reaction had a

certain catalytic activity. Figure S6a,b (Supplementary Materials) show the EIS patterns, whereby C/Co-FeS<sub>2</sub>/CoS<sub>2</sub> had a better conductivity with an improvement in performance.

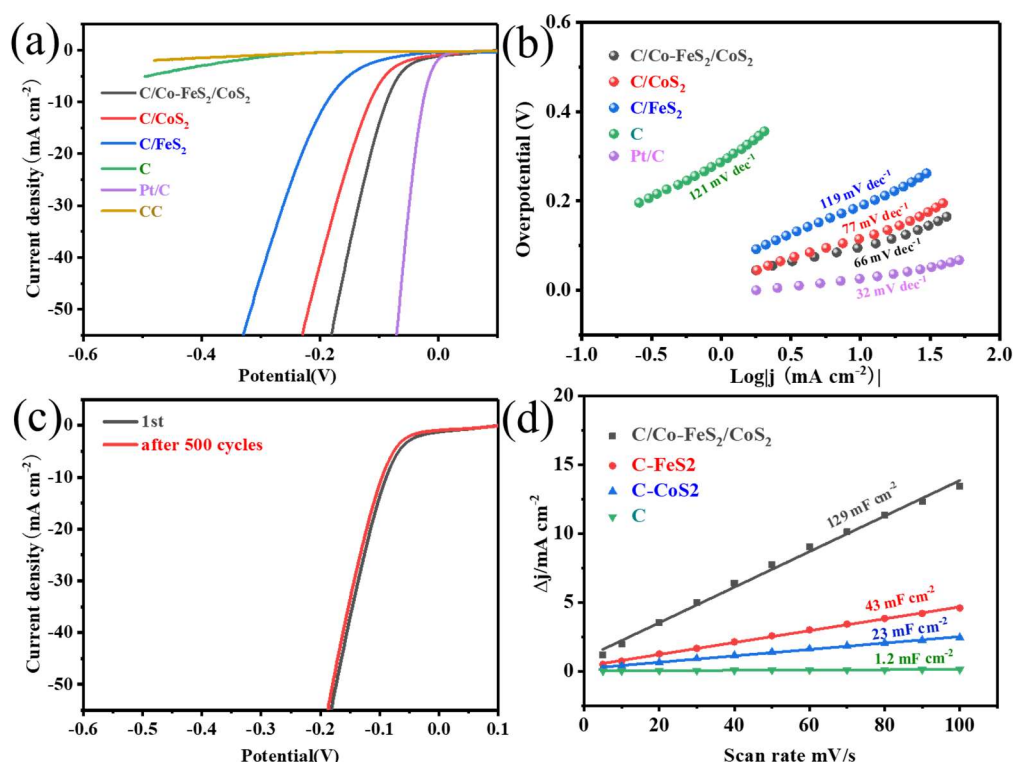


**Figure 4.** (a) LSV curves of C/Co-FeS<sub>2</sub>/CoS<sub>2</sub>, C/CoS<sub>2</sub>, C/FeS<sub>2</sub>, C, and bare CC for hydrogen evolution reaction (HER) in 0.5 M H<sub>2</sub>SO<sub>4</sub> solution. (b) The corresponding Tafel plots. (c) LSV curves before and after 500 CV cycles, and (d) corresponding ECSA.

### 3. Experimental Section

#### 3.1. Chemicals and Materials

The carbon cloth (CC) model purchased from CeTech Co., Ltd. was WOS1009 (Taiwan, China). The FeSO<sub>4</sub>·7H<sub>2</sub>O reagent used was sold by Shanghai Titan Technology Co., Ltd. (Shanghai, China). Co(NO<sub>3</sub>)<sub>2</sub>·6H<sub>2</sub>O, sulfur powder (S), thiourea (SC(NH<sub>2</sub>)<sub>2</sub>), Na<sub>2</sub>S·9H<sub>2</sub>O, C<sub>2</sub>H<sub>5</sub>OH, and H<sub>2</sub>SO<sub>4</sub> were obtained from Nanjing Chemical Reagent Co., Ltd. (Nanjing, China). Deionized water was obtained using a Millipore filter (Millipore Q, Raleigh, CA, USA).

#### 3.2. Synthesis of C/Co-FeS<sub>2</sub>/CoS<sub>2</sub>

Firstly, the appropriate size of carbon cloth (CC) was prepared, cleaned with deionized water and absolute ethanol, and then dried. Subsequently, FeSO<sub>4</sub>·7H<sub>2</sub>O (1.2 mM), Co(NO<sub>3</sub>)<sub>2</sub>·6H<sub>2</sub>O (0.156 mM), SC(NH<sub>2</sub>)<sub>2</sub> (1.8 mM), and C<sub>6</sub>H<sub>12</sub>O<sub>6</sub> (0.24 mM) were weighed out. The weighed reagent was added to a Teflon-lined autoclave (50 mL), and an appropriate amount of deionized water (25 mL) was added and stirred (15 min). After the first stirring, the sulfur powder (0.72 mM) was weighed and uniformly added into the reaction vessel and then slowly stirred (15 min). After the second stirring was completed, the prepared CC was inserted into the solution vertically. The reaction kettle was heated at 180 °C for 8 h. After the reaction was completed and cooled, the sample was taken out and cleaned with deionized water and absolute ethanol.

### 3.3. Synthesis of C/CoS<sub>2</sub>, C/FeS<sub>2</sub>, and C

Co(NO<sub>3</sub>)<sub>2</sub>·6H<sub>2</sub>O (1.2 mM), SC(NH<sub>2</sub>)<sub>2</sub> (1.8 mM), and C<sub>6</sub>H<sub>12</sub>O<sub>6</sub> (0.24 mM) were prepared for C/CoS<sub>2</sub>. FeSO<sub>4</sub>·7H<sub>2</sub>O (1.2 mM), SC(NH<sub>2</sub>)<sub>2</sub> (1.8 mM), and C<sub>6</sub>H<sub>12</sub>O<sub>6</sub> (0.24 mM) were prepared for C/FeS<sub>2</sub>. C<sub>6</sub>H<sub>12</sub>O<sub>6</sub> (1.2 mM) and SC(NH<sub>2</sub>)<sub>2</sub> (1.8 mM) were added to synthesis C. They were added to a 50-mL Teflon-lined autoclave; then, deionized water (25 mL) was added and stirred (15 min). Sulfur powder (0.72 mM) was then added and stirred (15 min) slowly for C/CoS<sub>2</sub> and C/FeS<sub>2</sub>. Stirring was stopped and the magnetic stirrer was removed. The cleaned and dried carbon fiber paper was inserted into the reactor solution vertically, and the reactor was heated at 180 °C for 8 h. After the reaction was completed and cooled, the sample was washed repeatedly with deionized water and ethanol.

### 3.4. Material Characterization

X-ray diffraction (XRD) patterns were collected using a Bruker D8 Advance X-ray diffractometer (XRD) with Cu-K $\alpha$  radiation (15° to 75°, 0.1°·s<sup>-1</sup>) (Bruker Daltonics Inc., Karlsruhe, Germany). Raman measurements were conducted using a Horiba LabRAM system (HORIBA, Ltd., Kyoto, Japan). SEM images were recorded on a field-emission scanning electron microscope (FE-SEM; JSM-7000F, JEOL Ltd., Tokyo, Japan). The elemental composition and distribution of the sample were investigated with an energy-dispersive spectrometer (EDS; Inca x-stream 034A0, Oxford Instruments KK, Tokyo, Japan). TEM and HRTEM images were recorded on a JEOL type JEM2100 instrument (JEOL Ltd., Tokyo, Japan). XPS was performed on the as-synthesized C/Co-FeS<sub>2</sub>/CoS<sub>2</sub> using a PHI5000 Versaprobe (Ulvac-Phi Inc., Kanagawa, Japan).

### 3.5. Electrochemical Measurements

The CHI760E electrochemical analyzer (CH Instruments, Chenhua Co., Shanghai, China) was used to analyze the performance of samples. The test uses a three-electrode system with the sample, a platinum electrode, and a saturated calomel electrode as the working electrode, counter electrode, and reference electrode, respectively. The measured potentials were converted to a reversible hydrogen electrode (RHE) ( $E(\text{RHE}) = E_{\text{Hg}/\text{Hg}_2\text{Cl}_2} + 0.241 + 0.0591 \text{ pH}$ ). The electrolyte solution used H<sub>2</sub>SO<sub>4</sub> solution (0.5 M). Prior to testing, nitrogen needed to be bubbled into H<sub>2</sub>SO<sub>4</sub> solution to remove oxygen from the solution. LSV was measured from -0.8 to 0 V at 2 mV·s<sup>-1</sup>. The Tafel slope was obtained by computing the LSV data. The CV was tested at different scan rates with a potential range of 0 to 0.20 V vs. RHE for HER, and the resulting data were used to calculate the ECSA. EIS measurements were carried on in a frequency range from 10<sup>5</sup> to 0.01 Hz with an alternating current (AC) voltage of 5 mV.

## 4. Conclusions

In summary, C/Co-FeS<sub>2</sub>/CoS<sub>2</sub> with superior performance was prepared successfully by doping carbon in a one-step hydrothermal method. The synergy between non-metallic elemental carbon and C/Co-FeS<sub>2</sub>/CoS<sub>2</sub>, as well as the optimization of conductivity, further enhanced the catalytic efficiency. We believe that the doping of non-metallic elements in the catalyst provides a simple, feasible, and effective direction for the preparation of highly efficient non-precious metal catalysts.

**Supplementary Materials:** The following are available online at <http://www.mdpi.com/2073-4344/9/6/556/s1>: Figure S1. (a) SEM image of C/Co-FeS<sub>2</sub>/CoS<sub>2</sub>; (b–e) corresponding EDS elemental mapping images; Figure S2. (a,d) SEM images of C/FeS<sub>2</sub>; (b,e) SEM images of C/CoS<sub>2</sub>; (c,f) SEM images of C; Figure S4. Contrast of HER activity using electrocatalysts of similar materials; Figure S5. (a–d) cyclic voltammograms of C/Co-FeS<sub>2</sub>/CoS<sub>2</sub>, C/FeS<sub>2</sub>, C/CoS<sub>2</sub>, and C were measured in the non-faradaic capacitance current range at scan rates of 5, 10, 20, 30, 40, 50, 60, 70, 80, 90, and 100 mV·s<sup>-1</sup>; Figure S6. EIS Nyquist plots of C/Co-FeS<sub>2</sub>/CoS<sub>2</sub>, C/FeS<sub>2</sub>, C/CoS<sub>2</sub>, and C; Figure S7. (a,b) SEM images of C/Co-FeS<sub>2</sub>/CoS<sub>2</sub>; (c,d) SEM images of C/Co-FeS<sub>2</sub>/CoS<sub>2</sub> after 500 cycles.

**Author Contributions:** The experiments and characterizations were carried out by Y.G., K.W., with the assistance of H.W., H.S. and X.X., under the guidance of S.Y. and Y.S., Y.G. and S.Y. wrote the manuscript and prepared all figures. Y.S. and S.Y. supervised and coordinated all the work.

**Funding:** This work was supported by the National Basic Research Program of China (2018YFA0209101), and the National Science Foundation of China (No. 61205057, No. 11574136).

**Conflicts of Interest:** The authors declare no competing financial interest.

## References

1. Faber, M.S.; Jin, S. Earth-abundant inorganic electrocatalysts and their nanostructures for energy conversion applications. *Energy Environ. Sci.* **2014**, *7*, 3519–3542. [[CrossRef](#)]
2. Roger, I.; Shipman, M.A.; Symes, M.D. Earth-abundant catalysts for electrochemical and photoelectrochemical water splitting. *Nat. Rev. Chem.* **2017**, *1*. [[CrossRef](#)]
3. Stamenkovic, V.R.; Strmcnik, D.; Lopes, P.P.; Markovic, N.M. Energy and fuels from electrochemical interfaces. *Nat. Mater.* **2016**, *16*, 57–69. [[CrossRef](#)]
4. Zhu, J.; Ni, Y. Phase-controlled synthesis and the phase-dependent HER and OER performances of nickel selenide nanosheets by an electrochemical deposition route. *Cryst. Eng. Commun.* **2018**, *20*, 3344–3352. [[CrossRef](#)]
5. Tang, C.; Gan, L.F.; Zhang, R.; Lu, W.B.; Jiang, X. Ternary  $\text{Fe}_x\text{Co}_{1-x}\text{P}$  nanowire array as a robust hydrogen evolution reaction electrocatalyst with Pt-like activity: Experimental and theoretical insight. *Nano Lett.* **2016**, *16*, 6617–6621. [[CrossRef](#)] [[PubMed](#)]
6. Xiong, W.; Guo, Z.; Li, H.; Zhao, R.; Wang, X.W. Rational bottom-up engineering of electrocatalysts by atomic layer deposition: A case study of  $\text{Fe}_x\text{Co}_{1-x}\text{S}_y$ -based catalysts for electrochemical hydrogen evolution. *ACS Energy Lett.* **2017**, *2*, 2778–2785. [[CrossRef](#)]
7. Zou, X.; Zhang, Y. Noble metal-free hydrogen evolution catalysts for water splitting. *Chem. Soc. Rev.* **2015**, *44*, 5148–5180. [[CrossRef](#)] [[PubMed](#)]
8. Wang, J.; Cui, W.; Liu, Q.; Xing, Z.; Asiri, A.M.; Sun, X. Recent progress in cobalt-based heterogeneous catalysts for electrochemical water splitting. *Adv. Mater.* **2016**, *28*, 215–230. [[CrossRef](#)]
9. Li, Y.J.; Zhang, H.C.; Jiang, M.; Zhang, Q.; He, P.L. 3D self-supported Fe-doped  $\text{Ni}_2\text{P}$  nanosheet arrays as bifunctional catalysts for overall water splitting. *Adv. Funct. Mater.* **2017**, *27*. [[CrossRef](#)]
10. Zhu, C.Z.; Fu, S.F.; Du, D.; Lin, Y.H. Facile tuning porous  $\text{NiCo}_2\text{O}_4$  nanosheets with metal valence-state alteration and abundant oxygen vacancies as robust electrocatalysts towards water splitting. *Chem. Eur. J.* **2016**, *22*, 4000–4007. [[CrossRef](#)]
11. Zang, Y.P.; Niu, S.W.; Wu, Y.S.; Zheng, X.S.; Cai, J.Y. Tuning orbital orientation endows molybdenum disulfide with exceptional alkaline hydrogen evolution capability. *Nat. Commun.* **2019**, *10*, 1217. [[CrossRef](#)] [[PubMed](#)]
12. Ma, R.G.; Zhou, Y.; Chen, Y.F.; Li, P.X.; Liu, Q. Ultrafine molybdenum carbide nanoparticles composited with carbon as a highly active hydrogen-evolution electrocatalyst. *Angew. Chem.* **2015**, *54*, 14723–14727. [[CrossRef](#)] [[PubMed](#)]
13. Wang, D.Y.; Gong, M.; Chou, H.L.; Pan, C.J.; Chen, H.A. Highly active and stable hybrid catalyst of cobalt-doped  $\text{FeS}_2$  nanosheets–carbon nanotubes for hydrogen evolution reaction. *J. Am. Chem. Soc.* **2015**, *137*, 1587–1592. [[CrossRef](#)] [[PubMed](#)]
14. Faber, M.S.; Lukowski, M.A.; Ding, Q.; Kaiser, N.S.; Jin, S. Earth-abundant metal pyrites ( $\text{FeS}_2$ ,  $\text{CoS}_2$ ,  $\text{NiS}_2$ , and their alloys) for highly efficient hydrogen evolution and polysulfide reduction electrocatalysis. *J. Phys. Chem. C* **2014**, *118*, 21347–21356. [[CrossRef](#)] [[PubMed](#)]
15. Li, Y.X.; Yin, J.; An, L.; Lu, M.; Sun, K.  $\text{FeS}_2/\text{CoS}_2$  interface nanosheets as efficient bifunctional electrocatalyst for overall water splitting. *Small* **2018**, *14*, 1801070. [[CrossRef](#)] [[PubMed](#)]
16. Yin, J.; Li, Y.X.; Lv, F.; Lu, M.; Sun, K. Oxygen vacancies dominated  $\text{NiS}_2/\text{CoS}_2$  interface porous nanowires for portable Zn-air batteries driven water splitting devices. *Adv. Mater.* **2017**, *29*, 1704681. [[CrossRef](#)] [[PubMed](#)]
17. Jasion, D.; Barforoush, J.M.; Qiao, Q.; Zhu, Y.; Ren, S.; Leonard, K.C. Low-dimensional hyperthin  $\text{FeS}_2$  nanostructures for efficient and stable hydrogen evolution electrocatalysis. *ACS Catal.* **2015**, *5*, 6653–6657. [[CrossRef](#)]
18. Faber, M.S.; Dziedzic, R.; Lukowski, M.A.; Kaiser, N.S.; Ding, Q. High-performance electrocatalysis using metallic cobalt pyrite ( $\text{CoS}_2$ ) micro- and nanostructures. *J. Am. Chem. Soc.* **2014**, *136*, 10053–10061. [[CrossRef](#)]
19. Wang, K.; Guo, W.L.; Yan, S.C.; Song, H.Z.; Shi, Y. Hierarchical  $\text{Co-FeS}_2/\text{CoS}_2$  heterostructures as a superior bifunctional electrocatalyst. *RSC Adv.* **2018**, *8*, 28684–28691. [[CrossRef](#)]

20. Wang, S.B.; Ding, Z.X.; Wang, X.C. A stable  $\text{ZnCo}_2\text{O}_4$  cocatalyst for photocatalytic  $\text{CO}_2$  reduction. *Chem. Commun.* **2015**, *51*, 1517–1519. [[CrossRef](#)]
21. Wang, H.; Zhuo, S.; Liang, Y.; Han, X.; Zhang, B. General self-template synthesis of transition-metal oxide and chalcogenide mesoporous nanotubes with enhanced electrochemical performances. *Angew. Chem.* **2016**, *128*, 9201–9205. [[CrossRef](#)]
22. Miao, R.; Dutta, B.; Sahoo, S.; He, J.; Zhong, W. Mesoporous iron sulfide for highly efficient electrocatalytic hydrogen evolution. *J. Am. Chem. Soc.* **2017**, *139*, 13604–13607. [[CrossRef](#)] [[PubMed](#)]
23. Xu, L.; Hu, Y.J.; Zhang, H.X.; Jiang, H.; Li, C.Z. Confined synthesis of  $\text{FeS}_2$  nanoparticles encapsulated in carbon nanotube hybrids for ultrastable lithium ion batteries. *ACS Sustain. Chem. Eng.* **2016**, *4*, 4251–4255. [[CrossRef](#)]
24. Zhou, W.J.; Jia, J.; Lu, J.; Yang, L.J.; Hou, D.M. Recent developments of carbon-based electrocatalysts for hydrogen evolution reaction. *Nano Energy* **2016**, *28*, 29–43. [[CrossRef](#)]
25. Yan, X.C.; Jia, Y.; Odedairo, T.; Zhao, X.J.; Jin, Z. Activated carbon becomes active for oxygen reduction and hydrogen evolution reactions. *Chem. Commun.* **2016**, *52*, 8156–8159. [[CrossRef](#)] [[PubMed](#)]
26. Li, Y.; Wang, J.; Tian, X.K.; Ma, L.L.; Dai, C. Carbon doped molybdenum disulfide nanosheets stabilized on graphene for hydrogen evolution reaction with high electrocatalytic ability. *Nanoscale* **2016**, *8*, 1676–1683. [[CrossRef](#)] [[PubMed](#)]
27. Chen, L.; Zhou, M.; Luo, Z.; Wakeel, M.; Asiri, A.M.; Wang, X. Template-free synthesis of carbon-doped boron nitride nanosheets for enhanced photocatalytic hydrogen evolution. *Appl. Catal. B-Environ.* **2019**, *241*, 246–255. [[CrossRef](#)]
28. Liu, Y.R.; Gou, J.X.; Li, X.; Dong, B.; Han, G.Q. Self-sacrificial template method of  $\text{Mo}_3\text{O}_{10}(\text{C}_6\text{H}_8\text{N})_2 \cdot 2\text{H}_2\text{O}$  to fabricate  $\text{MoS}_2$ /carbon-doped  $\text{MoO}_2$  nanobelts as efficient electrocatalysts for hydrogen evolution reaction. *Electrochim. Acta* **2016**, *216*, 397–404. [[CrossRef](#)]
29. Li, Y.M.; Shen, J.R.; Li, J.J.; Liu, S.M.; Yu, D.L. Constructing a novel strategy for carbon-doped  $\text{TiO}_2$  multiple-phase nanocomposites toward superior electrochemical performance for lithium ion batteries and the hydrogen evolution reaction. *J. Mater. Chem. A* **2017**, *5*, 7055–7063. [[CrossRef](#)]
30. Lin, H.L.; Zhang, W.B.; Shi, Z.P.; Che, M.W.; Yu, X. Electrospinning hetero-nanofibers of  $\text{Fe}_3\text{C}$ - $\text{Mo}_2\text{C}$ /nitrogen-doped-carbon as efficient electrocatalysts for hydrogen evolution. *Chem. Sustain. Chem.* **2017**, *10*, 2597–2604. [[CrossRef](#)]
31. Wei, H.F.; Xi, Q.Y.; Chen, X.A.; Guo, D.Y.; Ding, F. Molybdenum carbide nanoparticles coated into the graphene wrapping n-doped porous carbon microspheres for highly efficient electrocatalytic hydrogen evolution both in acidic and alkaline media. *Adv. Sci.* **2018**, *5*, 1700733. [[CrossRef](#)] [[PubMed](#)]
32. Zhao, J.X.; Chen, Z.F. Carbon-doped boron nitride nanosheet: An efficient metal-free electrocatalyst for the oxygen reduction reaction. *J. Phys. Chem. C* **2015**, *119*, 26348–26354. [[CrossRef](#)]
33. Schwan, J.; Ulrich, S.; Batori, V.; Ehrhardt, H.; Silva, S.R.P. Raman Spectroscopy on Amorphous Carbon Films. *J. Appl. Phys.* **1996**, *80*, 440–447. [[CrossRef](#)]
34. Chen, Y.; Xu, S.; Li, Y.; Jacob, R.J.; Kuang, Y.; Liu, B.  $\text{FeS}_2$  nanoparticles embedded in reduced graphene oxide toward robust, high-performance electrocatalysts. *Adv. Energy Mater.* **2017**, *7*, 1700482. [[CrossRef](#)]
35. Huang, S.Y.; Sodano, D.; Leonard, T.; Luisom, S.; Fedkiw, P.S. Cobalt-doped iron sulfide as an electrocatalyst for hydrogen evolution. *J. Electrochem. Soc.* **2017**, *164*, 276–282. [[CrossRef](#)]

